Nanoscale

PAPER

View Article Online
View Journal | View Issue

Cite this: *Nanoscale*, 2018, **10**, 16657

Synthesis of germanium–platinum nanoparticles as high-performance catalysts for spray-deposited large-area dye-sensitized solar cells (DSSC) and the hydrogen evolution reaction (HER)†

Suh-Ciuan Lim,‡[a] Ming-Cheng Hsiao,‡[a] Ming-De Lu,[b] Yung-Liang Tung[b] and Hsing-Yu Tuan *[a]

Received 17th May 2018,
Accepted 14th August 2018

DOI: 10.1039/c8nr03983f

rsc.li/nanoscale

$GePt_3$ and Ge_2Pt nanoparticles were synthesized *via* a solution colloidal method as catalysts for dye-sensitized solar cells (DSSC) and the hydrogen evolution reaction (HER). The shape, size, arrangement, phases and crystalline structures of Ge–Pt nanoparticles were determined, and the ability to be dispersed in nonpolar solvents enabled them to form a catalyst ink with a stable ejection for the spray coating technique. A series of electrochemical analyses confirmed the catalytic properties of Ge–Pt nanoparticles toward the I^-/I_3^- redox reaction system. The DSSC using $GePt_3$ nanoparticles as the counter electrode exhibited excellent power conversion efficiency (PCE) of 8.04% at 0.16 cm^2, which was comparable to that of a DSSC using Pt as the counter electrode (8.0%); it also exhibited an average PCE of 7.26% even at a large working area (2 cm^2). In addition, the $GePt_3$ catalyst exhibited excellent HER electrocatalytic performance with a large current density and a low Tafel slope, and it could stably operate at a working area of up to 5 cm^2 with a low over potential (<0.06 V) to achieve 10 mA cm^{-2} cathodic current. This study provides fundamental insights into the preparation of germanium–platinum intermetallic compound catalysts at the nanoscale, which can be beneficial for the design and development of clean energy devices.

1. Introduction

Platinum (Pt) group nanomaterials attract growing interest due to their unique electronic properties, atomically ordered crystal structures and high catalytic activities[1–3] as well as their important applications as a counter electrode material for dye-sensitized solar cells (DSSCs) or as an active catalyst for the hydrogen evolution reaction (HER), hydrogenation, methanol oxidation and oxygen reduction reaction (ORR).[4–8] However, the high cost and low natural abundance essentially limit their large-scale applications. Thus, many scientific efforts have recently been devoted to incorporate other metals into Pt nanostructures such as SnPt, FePt, $CoPt_3$, NiPt, MnPt, PdPt, $TiPt_3$, VPt_3, $CuPt_3$ and ZnPt[9–18] with the aim of decreasing the Pt usage while increasing the catalysts' activities and long-term stability. It has been proved that improved activities normally result due to some synergetic effects including electronic and geometric effects, which originate from the lattice contraction and the downshift of the d-band center of Pt in the Pt compound.[19]

Elemental germanium nanoparticles have been applied widely in fibre-optic systems, infrared optics, and as catalysts for the polymerization reaction as well as in solar cells and energy storage.[20–23] They can form diverse compounds or alloys with various elements. These germanium (Ge) compounds are used as highly reactive reagents (NaGe, KGe, $GeBr_2$), magnetic materials (FeGe, CoGe), optical and catalytic materials (Ge_3N_4, GeS, GeSe) and non-volatile phase change materials for memory devices (GeTe, GeSbTe).[20,24–26] Moreover, the applications and the significance of silicon–germanium compounds as sensitive layers in integrated circuit (IC) are also well-known.[27,28]

The Ge–Pt intermetallic compound system includes six phases: GePt, $GePt_2$, $GePt_3$, Ge_2Pt, Ge_2Pt_3 and Ge_3Pt_2.[29] In this system, the electrophilic character of platinum can be increased by germanium, which acts as an electron-acceptor,[30] resulting in the generation of unique catalytic properties. Recently, the investigation of the applications of Ge–Pt inter-

[a]*Department of Chemical Engineering, National Tsing Hua University, 101, Section 2, Kuang-Fu Road, Hsinchu, Taiwan 30013, Republic of China. E-mail: hytuan@che.nthu.edu.tw*

[b]*Green Energy & Environment Research Laboratories, Industrial Technology Research Institute, 195, Sec. 4, Chung Hsing Rd., Chutung, Hsinchu, Taiwan 31040, Republic of China*

†Electronic supplementary information (ESI) available. See DOI: 10.1039/c8nr03983f

‡These authors contributed equally to this work.

metallic compounds or Ge–Pt supported on carbon as electrocatalysts for CO oxidation and fine chemistry hydrogenation reactions have attracted great attention.[31–33] In addition, previous reports show that Ge–Pt can prevent coke deposition on contiguous Pt surfaces in some of the naphtha reforming catalyst reactions.[34] However, there is still a lack of studies on the catalytic properties of Ge–Pt intermetallic compounds at the nanoscale. We herein demonstrate the first example of a colloidal synthetic approach to obtain crystalline Ge_2Pt and $GePt_3$ nanoparticles with well-defined shapes. During the synthesis, oleic acid (OA) or trioctylphosphine (TOP) ligands play an important role for single crystal formation,[35,36] and the decomposition of Pt and Ge precursors in the nucleation step is critical to produce monodisperse nanoparticles.[37] The as-synthesized well-dispersed nanoparticles can form a catalyst ink in a nonpolar solvent with a stable ejection for the spray coating technique. We experimentally show that the DSSC using $GePt_3$ nanoparticles as the counter electrode exhibits an excellent power conversion efficiency (PCE) of 8.04% at 0.16 cm^2, which is comparable to that of the DSSC using Pt as the counter electrode (8.0%); it also exhibits an average PCE of 7.26% even at a large working area (2 cm^2). Overall, our results show that the $GePt_3$ nanoparticle-based DSSC cell can achieve a relatively low short-circuit current (~27 mA) and an open-circuit voltage (~0.7 V). On the other hand, when evaluated for the HER performance, $GePt_3$ nanoparticles exhibit improved performance compared to conventional Pt (0.033 V at 0.07 cm^2 and 0.024 V at 0.2 cm^2) and excellent long-term cycling stability in an acidic electrolyte. Finally, the HER area is enlarged to 5 cm^2, and it can provide sufficient hydrogen to successfully operate a fuel cell system.

2. Experimental section

2.1 Synthesis of platinum–germanium alloy nanoparticles

For the synthesis of $GePt_3$, 0.1 mmol of platinum(II) iodide (PtI_2, 0.0464 g), 0.5 mL of OA and 6 mL of oleylamine (OLA) were added into a 50 mL three neck flask and connected to the Schlenk line system. The argon-filled three-neck flask was preheated for 30 minutes at 130 °C. Meanwhile, 0.035 mmol of germanium(IV) iodide (GeI_4, 0.02 g), 0.25 mL of OA and 3 mL of OLA were added to a sample vial and sonicated until dissolution. The solution was then injected into the three-neck flask along with 0.5 mL of hexamethyldisilazane (HMDS) and reheated to 130 °C. The system was then heated up to 260 °C by 2 °C min^{-1} and cooled down instantly to room temperature with a cold water bath. The as-synthesized nanoparticles were then washed by adding 5 mL toluene and 10 mL ethanol followed by centrifugation at 8000 rpm for 5 min three times, and the byproduct and the unreacted precursors were discarded. For the synthesis of Ge_2Pt, 0.1 mmol of PtI_2 (0.0464 g), 0.5 mL of TOP and 6 mL of OLA were added to a 50 mL three neck flask and connected to the Schlenk line system. The argon-filled three-neck flask was preheated for 30 minutes at 130 °C. Meanwhile, 0.1 mmol of GeI_4 (0.06 g), 0.75 mL of OA and 10 mL of OLA were added to a sample vial and sonicated until dissolution. The solution was then injected into the three-neck flask along with 0.5 mL of HMDS and reheated to 130 °C. The system was then heated up to 320 °C by 2 °C min^{-1} and cooled down instantly to room temperature with a cold water bath. The as-synthesized nanoparticles were then washed by adding 5 mL of toluene and 10 mL of ethanol followed by centrifugation at 8000 rpm for 5 min three times, and the byproduct and the unreacted precursors were discarded.

2.2 Characterization

The morphology and structure of the as-prepared nanoparticles were characterized by scanning electron microscopy (SEM, Hitachi SU8010). Transmission electron microscopy (TEM, Hitachi H-7100) was conducted for the further analysis of shape, size and crystalline phase. XRD data were obtained by a Rigaku Ultima IV X-ray diffractometer using a Cu radiation source (λ = 1.54 Å). An inductively coupled plasma mass spectrometry (ICP-MS) analysis was performed on Agilent 7500ce (Agilent Technologies, Tokyo, Japan). X-ray photoelectron spectroscopy (XPS) measurement was performed using ULVAC-PHI high resolution XPS equipped with monochromatized Al Kα (1486.6 eV) excitation.

2.3 DSSC counter electrode preparation

Typically, ~30 mg of $GePt_3$ or Ge_2Pt nanoparticles was dispersed in 10 ml toluene and sonicated for 30 min to prepare the catalyst ink. By spray coating, a thin layer of the electrocatalyst was deposited on the fluorine-doped tin oxide (FTO) glass substrate (SnO_2: F glass, 8 Ω per square). Next, the resultant thin layer was sintered at 400 °C in an argon atmosphere for 2 hours by the chemical vapor deposition (CVD) method. For comparison, a standard Pt-based DSSC was also fabricated. For Pt counter electrode fabrication, a drop of plastisol (T/SP) solution was screen-printed onto FTO and incubated at 385 °C for 30 minutes.

2.4 DSSC assembly and measurements

A dye-adsorbed photoanode was fabricated using a screen-printed N719 dye-sensitized TiO_2 film with thickness of 14–16 μm. The TiO_2 film was then irradiated by UV light for 20 minutes and was soaked overnight in a mixed solution of acetonitrile and *tert*-butyl alcohol (1 : 1 (v/v)) containing 5×10^{-4} M N719 dye. Next, a spacer was inserted between the dye-adsorbed photoanode and the Ge–Pt- or Pt-coated FTO counter electrode, and the films were firmly clamped together. The redox electrolyte (0.05 M I_2, 0.1 M LiI, 0.6 M 1,2-dimethyl 1-3 propylimidazolium iodide (DMPII) and 0.5 M 4-*tert*-butylpyridine in acetonitrile) was injected into the interspace between the photoanode and the counter electrode through a predrilled hole. Finally, DSSCs were sealed with epoxy resin under heat. The Tafel polarization measurement was performed using an electro-chemical working system (Bio-Logic-science Instruments, VMP3) in a symmetrical cell with the scan range of 20–200 mV s^{-1}. For cyclic voltammetry (CV)

measurements, Pt and Ag/Ag^+ electrodes were applied as the counter and the reference electrodes. The resultant CV curves were recorded between 1.0 V and −1.0 V with a scan rate of 50 mV s^{-1} in an acetonitrile-based electrolyte containing 10.0 mM LiI, 1.0 mM I_2 and 0.1 M $LiClO_4$. The performance of DSSC was then measured under simulated sunlight (AM 1.5 illumination). Electrochemical impedance spectroscopy was applied to determine the charge transfer resistance (R_{ct}) under solar simulation in the range of 0.1–100 kHz.

2.5 HER working electrode fabrication and measurements

A thin nanoparticle-based catalyst layer was deposited by the drop coating method for a small area, and the spray coating method was used for a large area. For the catalyst ink preparation, 0.020 g of the prepared Ge–Pt nanoparticles and a commercial Pt catalyst were dispersed in 5 mL of a mixed solvent containing tetrahydrofuran (THF), 2-propanol, and 5% Nafion (volume ratio was 3 : 1 : 0.1) and sonicated for 30 min. The working electrode was prepared by depositing 0.2 mg cm^{-2} of the catalyst ink on a glassy carbon electrode or a rotating disk electrode (RDE, Pine Instruments, d = 0.5 cm) and drying at room temperature. All electrochemical experiments were carried out on the VMP3 electrochemical workstation with a conventional three electrode system at room temperature. A platinum wire was used as the counter electrode, and a reversible hydrogen electrode (RHE, ALS) was employed as the reference electrode. Also, 0.5 M highly pure H_2-saturated H_2SO_4 aqueous solution was used as the supporting electrolyte for all the experiments. The LSV curves were recorded in the range from 0.3 V to −0.3 V at a scan rate of 5 mV s^{-1}, and the long-term durability test data were recorded at a stable voltage of −0.1 V *vs.* RHE over 12 h in 0.5 M H_2SO_4 with the electrode rotation of 2800 rpm. For the cycling durability test, ~30 cycles were performed in 0.5 M H_2SO_4 solution before the measurement to remove the residual surfactants in the voltage range from −0.3 to 0.2 V *vs.* RHE at 120 mV s^{-1} scan rate. The resultant CV curves were recorded between −0.3 and 0.2 V *vs.* RHE at 120 mV s^{-1} scan rate with the electrode rotation of 2800 rpm for 10 000 cycles.

3. Results and discussion

The colloidal synthesis process of Ge_2Pt and $GePt_3$ nanoparticles is depicted in Fig. 1(a). Iodide compounds were used for both germanium and platinum precursors, whereas OLA and OA were applied as the synthetic mixture or reducing (capping) agents. Fig. S1† shows the equilibrium diagram of the Ge–Pt system, indicating that the Ge–Pt compound could particularly form six types of phases.[29] Typical powdered X-ray diffraction (XRD) was applied as a bulk analysis technique to ensure compositional homogeneity of the $GePt_3$ nanoparticles. Fig. 2(a) shows the major reflections at 2θ values corresponding to (220), (113), (222), (400), (313) and (440) planes of an orthorhombic structure. Most peaks could be well indexed and matched well with the previously reported $GePt_3$ case

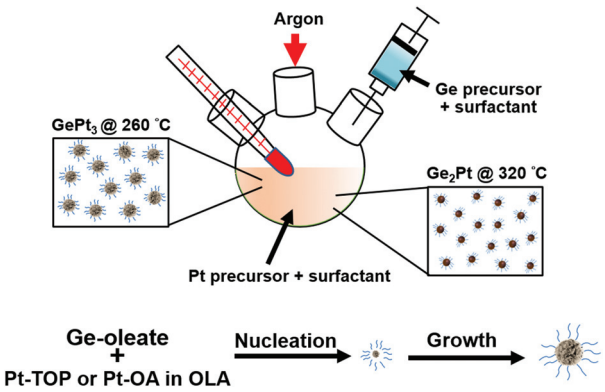

Fig. 1 (a) Schematic illustration of the synthesis of Ge–Pt nanocrystals.

(JCPDS no. 89-3026). Fig. 2(b) shows the simulated structural demonstration of crystalline monoclinic $GePt_3$ with the lattice constants of a = 7.92 Å, b = 7.77 Å, and c = 5.52 Å. The detailed morphology and structure of $GePt_3$ nanoparticles were further investigated by scanning electron microscopy (SEM) and transmission electron microscopy (TEM). Fig. 2(c) and (d) show the representative SEM image and the relative low magnification TEM result of the as-synthesized $GePt_3$ nanoparticles. $GePt_3$ nanoparticles formed spherical clusters with an average particle size of 55.4 ± 3.8 nm (Fig. 2(d), inset). The corresponding selected area electron diffraction (SAED) pattern (Fig. 2(e)) showed rings that matched the peaks of the XRD pattern, which verified the face-centered monoclinic (FCM)-type crystalline structure of $GePt_3$. Interestingly, when an individual $GePt_3$ nanocrystal was observed under TEM, the morphology showed a popcorn shape with uneven surfaces (Fig. 2(f)) (for more details on $GePt_3$ nanoparticle morphology, please refer to Fig. S2†). High-resolution transmission electron microscopy (HRTEM) images (Fig. 2(g–j)) showed two directions with the associated fast Fourier transform (FFT) of $GePt_3$ nanocrystals along the zone axis of [100] and [001] directions; the lattice fringes of the nanoparticles referring to $GePt_3$ lattice images indicated the (002) and (220) planes with the corresponding interplanar spacings of 0.39 nm and 0.28 nm. Also, from the HRTEM analysis, nanodendrites forming convex–concave surface structures covering $GePt_3$ nanoparticles could be clearly observed. It is believed that these structures may be due to a large number of stacking faults or convex atoms with low coordination numbers exposed on the surface, providing a high number of active sites.[38,39] Notably, the fragmental surfaces in HRTEM images (Fig. 2(g–j)) were assigned to exposed multiple facets including (220), (040), and (002) that resulted from high-density atomic steps, kinks, edges and dangling bonds, which exhibited higher catalytic activity, as reported by previous studies.[40–43]

Ge_2Pt nanocrystals were synthesized by adding a small amount of the reducing (capping) agent trioctylphosphine (TOP) and altering the final reaction temperature to 320 °C. Under XRD analysis, the diffraction peaks including (110), (200), (011), (220), (211) and (121) could be clearly observed

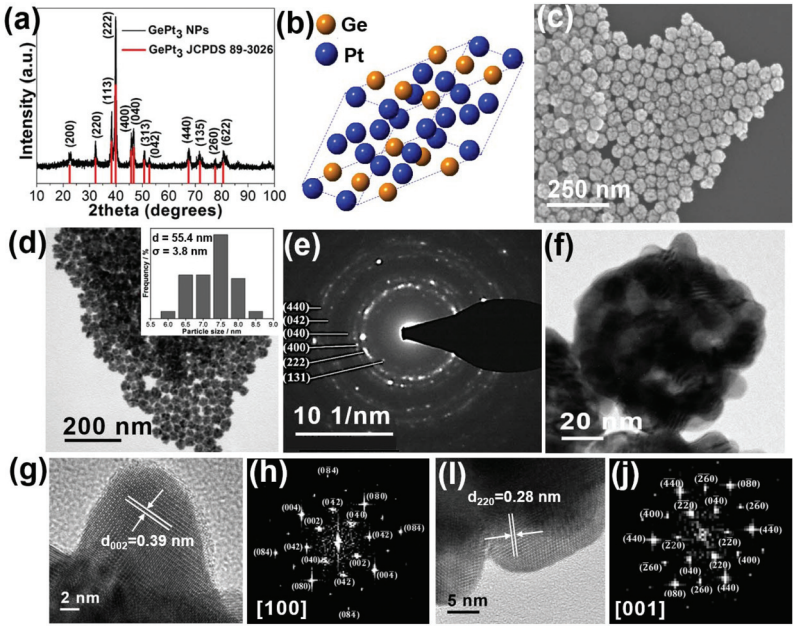

Fig. 2 $GePt_3$ nanocrystals: (a) XRD spectrum (b) simulated $GePt_3$ unit cell (c) SEM image (d) low magnification TEM image (inset: size distribution) (e) SAED pattern (f) a typical TEM image of an individual nanocrystal (g–j) HR-TEM images of the as-prepared $GePt_3$ nanocrystals and their corresponding FFT patterns.

(Fig. 3(a)), which matched well with that of the monoclinic structure of previously reported bulk Ge_2Pt (JCPDS no. 89-3029). Fig. 3(b) shows the simulated structure of orthorhombic Ge_2Pt with the lattice parameters of a = 6.19 Å, b = 5.77 Å, and c = 2.91 Å. TEM analysis results with different levels of magnifications successfully demonstrated classic spherical morphology, monodispersity and self-arrangement behavior of Ge_2Pt nanoparticles (Fig. 3(c) and (d)) (please refer to Fig. S3† for more details on SEM and TEM analyses). Ge_2Pt nanoparticles with an average particle size of 7.3 nm (Fig. 3(c), inset) and their uniform morphology could be controlled.[44] It is possible that the capping or reducing agent applied during the synthesis reaction caused the different shapes of the nanoparticles. For the synthesis of $GePt_3$, OA was applied since OLA readily desorbs from the nanoparticle surface owing to it being a relatively weak ligand; thus, $GePt_3$ nanoparticles were prone to agglomeration during reactions at high temperature, resulting in the formation of irregular-shaped (popcorn-shaped) particles.[45] On the other hand, this also indicated that the nanoparticles formed in the presence of TOP were spherical in shape, and their size decreased with an increase in the TOP/precursor ratio.[46] Please note that sufficient TOP was added as the capping agent during the synthesis process of Ge_2Pt. This trend was quite consistent with the results of TOP addition as it is a very effective additive for controlling the size and shape (small, spherical) of Ge_2Pt nanoparticles. The detailed crystalline structure of Ge_2Pt nanoparticles was further analyzed by HRTEM (Fig. 3(e) and (f)), and the associated FFT of the nanocrystals confirmed the as-synthesized product. The d-spacing between two lattice fringes was calculated to be 0.29 nm from the HRTEM images, which clearly indicated the presence of

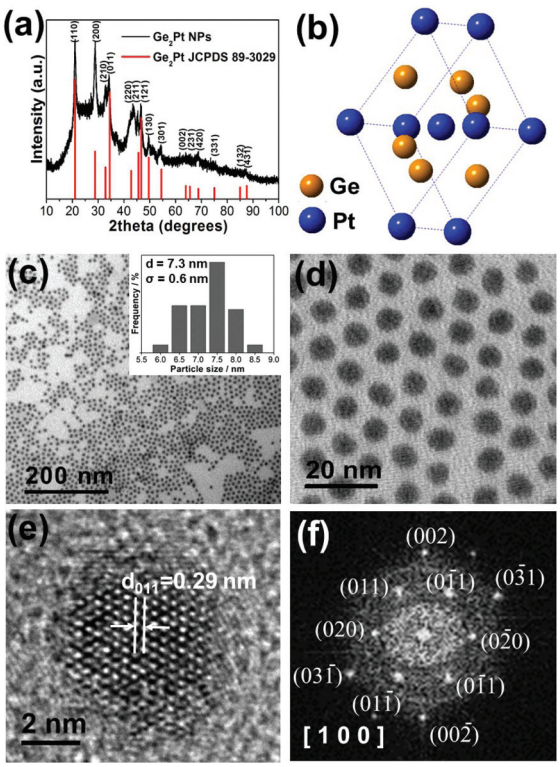

Fig. 3 Ge_2Pt nanocrystals: (a) XRD spectrum (b) simulated unit cell (c) low magnification TEM image (inset: size distribution) (d) high magnification TEM image (e–f) HR-TEM images of the as-prepared Ge_2Pt nanoparticles and the corresponding FFT patterns.

the (011) plane with [100] zone axes of ordered Ge_2Pt nanoparticles. Energy dispersive spectroscopy (EDS) analysis under TEM analysis further confirmed the stoichiometry of the as-synthesized nanoparticles. As shown in Fig. S4,† the elemental ratio of Ge : Pt was close to 1 : 3 for $GePt_3$, and the elemental ratio of Ge : Pt was about 2 : 1 for Ge_2Pt.

X-ray photoelectron spectroscopy (XPS) was used to investigate the nature of bonding, electronic structure and the chemical environment of constituent elements on the surface of Ge–Pt compounds. Peak energies were calibrated to adventitious carbon's C 1s peak centered at 284.8 eV (Fig. S5†). The Ge $3d_{5/2}$ peaks were at about 30.1 and 29.6 eV for $GePt_3$ and Ge_2Pt, respectively (Fig. 4(a) and (c)), which slightly upshifted compared to that of the conventional Ge powder (29.3 eV),[47] indicating the presence of a bimetallic compound and the modification of electronic structures due to alloying of Ge with Pt.[48] The presence of a significant amount of GeO_2 in Ge_2Pt was not surprising and seemed to be unavoidable due to the gradual oxidation of Ge or oxidized germanium chemisorbed on Pt during air exposure.[49–51] As shown in Fig. 4(b) and (d), after the formation of the Ge–Pt alloy, the Pt 4f binding energy of Pt–Ge clearly blue-shifted compared to that of conventional Pt.[52–54] The peaks of Pt $4f_{7/2}$ and Pt $4f_{5/2}$ in the spectrum of Pt were located at 71.2 and 74.5 eV for $GePt_3$ and at 71.1 and 74.4 eV for Ge_2Pt, respectively.

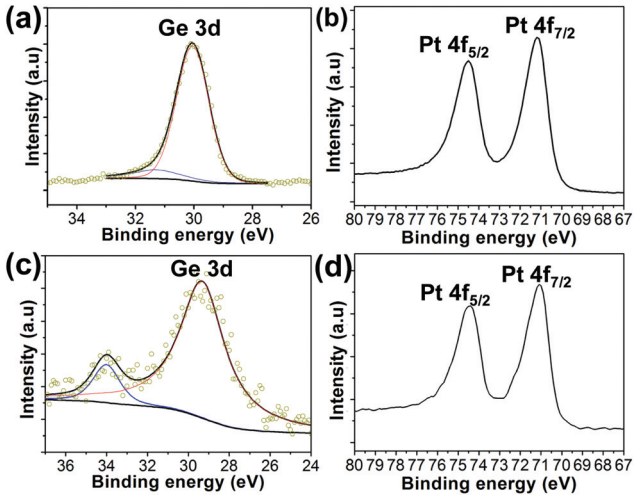

Fig. 4 XPS spectra of $GePt_3$ (a) Ge 3d (b) Pt 4f and Ge_2Pt (c) Ge 3d (d) Pt 4f.

Fig. S6† shows the assembled DSSCs with two different reaction areas in this study. The band structure of a Ge_2Pt or $GePt_3$ counter electrode-based DSSC is described in Fig. 5(a), and the measured work functions of $GePt_3$ and Ge_2Pt thin films were 4.51 eV and 4.38 eV, respectively; both these values were close to the previously reported value for graphene layer (4.5 eV).[55,56] To experimentally investigate the catalytic activities of the counter electrodes, we applied cyclic voltammetry (CV) analysis at a scan rate of 50 mV s^{-1} in a acetonitrile-based electrolyte containing 10 mM LiI, 1.0 mM I_2 and 0.1 M $LiClO_4$. Fig. 5(b) shows two pairs of prominent redox peaks, where peaks α and β represent two oxidation steps corresponding to eqn (1) and (2).[57]

$$3I^- \rightarrow I_3^- + 2e^- \quad (1)$$

$$2I_3^- \rightarrow 3I_2 + 2e^- \quad (2)$$

Eqn (1) and (2) show the oxidization reaction of iodide to tri-iodide (peak α) and the oxidization reaction of tri-iodide to iodine (peak β). In reverse reactions, peaks α′ and β′ represent two reduction steps corresponding to eqn (3) and (4).

$$3I_2^- \rightarrow 2e^- \rightarrow 2I_3^- \quad (3)$$

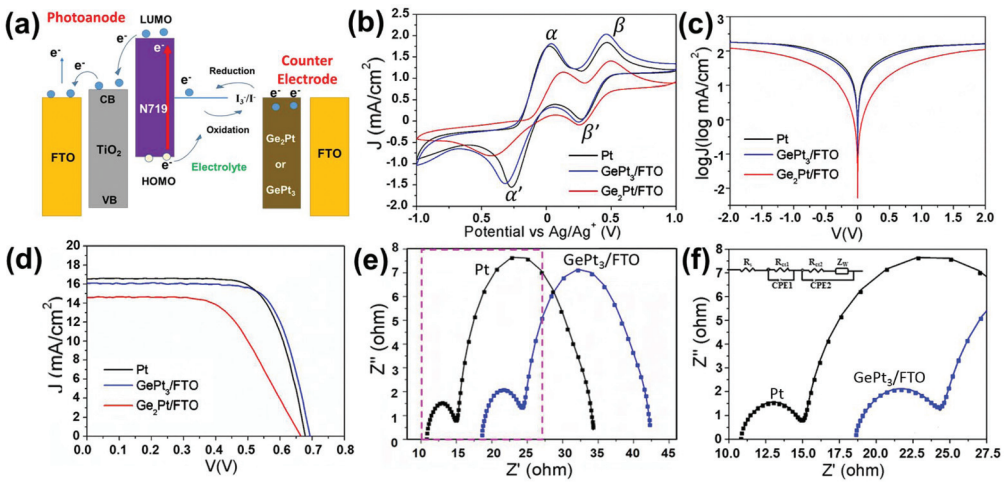

Fig. 5 (a) Band structure of a Ge_2Pt or $GePt_3$ counter electrode-based DSSC. (b) Cyclic voltammograms of Pt wafer, $GePt_3$-coated FTO, and Ge_2Pt-coated FTO substrate for the I_2/I^- system. (c) Tafel polarization curves of I^-/I_3^- symmetrical cells of Pt, $GePt_3$/FTO and $GePt_2$/FTO substrates. (d) *J–V* curves of the 0.16 cm^2 DSSC with Pt, $GePt_3$-coated FTO, and Ge_2Pt-coated FTO. (e–f) Nyquist plots of the 0.16 cm^2 DSSC with Pt and $GePt_3$-coated FTO.

$$I_3^- + 2e^- \rightarrow 3I^- \quad (4)$$

Eqn (3) and (4) show the reduction reaction of iodine to tri-iodide (peak β′) and the reduction reaction of tri-iodide to iodide (peak α′). Next, we employed the Tafel polarization measurement to estimate interfacial charge-transfer properties on the electrode surface. The measured Tafel curves of Pt, $GePt_3$ and Ge_2Pt electrodes by symmetrical dummy cells are shown in Fig. 5(c); the relative R_{ct} values can be obtained from eqn (5):[58]

$$J_0 = \frac{RT}{nFR_{ct}} \quad (5)$$

In the above equation, R represents the gas constant, T represents the temperature, n represents the total number of electrons involved in the reaction, F represents the Faraday's constant, J_0 represents the exchange current density and R_{ct} is the direct measurement of the electron exchange ability between the electrode and the electrolyte;[59,60] also, J_0 is inversely proportional to R_{ct} (Fig. S8†). Next, we applied the nanoparticles to DSSC devices as the cathode with a working area of 0.16 cm^2. Fig. 5(d) shows the photocurrent density–voltage (J–V) curves of Pt, $GePt_3$/FTO and Ge_2Pt/FTO when applied as the counter electrodes of DSSC. All photovoltaic parameters of DSSCs are summarized in Table 1, and the results indicated that the $GePt_3$/FTO counter electrode exhibited an average power-conversion efficiency (PCE) of 8.04%, which was comparable to that of the DSSC using Pt as the counter electrode (8.0%). This demonstrated that the reactions of I^{3-}/I^- redox pairs could be enhanced by using $GePt_3$ as the counter electrode. In addition, the good performance might be due to the higher Pt molecular ratio in $GePt_3$ nanoparticles. In addition, our data showed that R_{ct} of the $GePt_3$/FTO counter electrode was slightly higher than that of Pt (Fig. 5(e and f)). The open circuit voltages (V_{oc}) of Pt, $GePt_3$/FTO, or Ge_2Pt/FTO-based DSSCs were around 0.68 to 0.70 V; please note that the DSSC using $GePt_3$ as the counter electrode exhibited a lower fill factor (FF) and higher R_{ct} than Pt since its short-circuit current density was slightly lower.

Both Ge_2Pt and $GePt_3$ nanoparticles were well dispersed in nonpolar solvents, forming catalyst inks that can be applied for stable ejections (Fig. 6(a)).[61] For the nanoparticle films, sintering process is important for the removal of surfactants from nanoparticles. After annealing for 2 hours in an argon atmosphere at 400 °C, both $GePt_3$ and Ge_2Pt nanocrystals could

Table 1 Photovoltaic performances of 0.16 cm^2 DSSCs with Pt, $GePt_3$/FTO, and Ge_2Pt/FTO counter electrodes

	V_{oc} (V)	J_{sc} (mA cm^{-2})	FF	PCE (%)	R_s (Ω)	R_{ct} (Ω)
Pt-1	0.68	16.55	0.73	8.02	10.77	4.42
Pt-2	0.69	16.37	0.74	7.98	—	—
$GePt_3$/FTO-1	0.70	16.09	0.72	8.10	18.49	6.18
$GePt_3$/FTO-2	0.72	16.25	0.70	8.05	11.24	5.43
$GePt_3$/FTO-3	0.69	16.54	0.69	7.96	—	—
Ge_2Pt/FTO	0.69	14.58	0.58	5.65	—	—

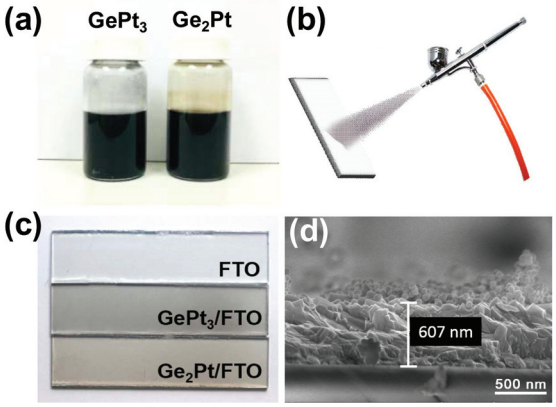

Fig. 6 (a) Catalyst inks of $GePt_3$ and Ge_2Pt nanoparticles. (b) Process of spray coating an FTO substrate to assemble DSSCs with a reactive area of 2 cm^2. (c) Corresponding FTOs after spray coating. (d) Cross-sectional SEM image of $GePt_3$ on FTO.

form a thin layer when applied onto suitable substrates. Fig. 6(b) shows the process of spray coating. By this strategy, Ge_2Pt and $GePt_3$ nanoparticles could form a transparent layer on FTO with a coating thickness of ~600 nm (Fig. 6(c) and (d)). Fig. S7† shows the uniform distribution of spray-coated $GePt_3$ nanoparticles on an FTO surface for DSSC applications. Next, the working area of the counter electrodes for DSSC devices was enlarged to 2 cm^2 and thus produced higher interior resistance. Fig. 7(a) shows the J–V curves of DSSCs using different counter electrodes, and all the photovoltaic parameters of

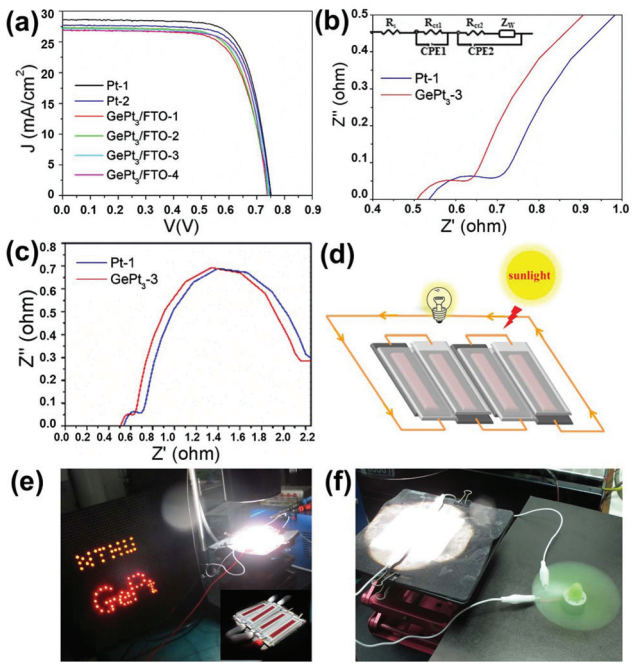

Fig. 7 (a) J–V curves of 2 cm^2 DSSCs with Pt and $GePt_3$-coated FTO. (b–c) Nyquist plots of 2 cm^2 DSSCs with Pt and $GePt_3$-coated FTO. (d) Schematic diagram of series-connected DSSCs. (e–f) Demonstration of a $GePt_3$-based series-connected DSSC application.

Table 2 Photovoltaic performances of 2 cm^2 DSSCs with Pt and $GePt_3$/FTO counter electrodes

	V_{oc} (V)	J_{sc} (mA cm^{-2})	FF	PCE (%)	R_s (Ω)	R_{ct} (Ω)
Pt-1	0.752	14.29	0.736	7.9	0.53	0.17
Pt-2	0.75	13.86	0.735	7.64	—	—
$GePt_3$/FTO-1	0.747	13.46	0.702	7.06	—	—
$GePt_3$/FTO-2	0.742	13.66	0.713	7.23	—	—
$GePt_3$/FTO-3	0.746	13.58	0.727	7.37	0.51	0.12
$GePt_3$/FTO-4	0.738	13.49	0.742	7.38	—	—

DSSC devices with 2 cm^2 counter electrodes are summarized in Table 2. It was found that the DSSC using Pt as the counter electrode still exhibited a relatively high average PCE (7.26%). The decreasing photovoltaic parameters in DSSCs could be due to the increasing working area. Fig. 7(b) and (c) and Table 2 show that similar series resistance (R_s) results were found for the DSSC using Pt as the counter electrode and the DSSC using $GePt_3$ as the counter electrode (0.51 and 0.53 Ω). Next, the DSSCs using $GePt_3$ as the counter electrode were tested by applying onto certain electronic devices (Fig. 7(e) and (f)). The $GePt_3$-based DSSC with a reactive area of 2 cm^2 could generate a short current of ~27 mA. However, the open-circuit voltage of each cell (~0.6 V) was too low to drive an electronic device; therefore, four DSSCs were connected in series to achieve an open-circuit voltage of 2.4 V (Fig. 7(d)). As an example of demonstration, $GePt_3$-based DSSCs were series-connected to a light-emitting diode (LED) board containing ~70 yellow and red LED bulbs. It successfully lit the LED bulbs without fading for a certain time (Fig. 7(e) and Fig. S9(a), Movie S1†). The $GePt_3$-based DSSC array was then further applied to an electric fan. As long as the illumination kept the DSSC array functioning, the electric fan kept spinning (Fig. 7(f) and Fig. S9(b), Movie S2†). A higher current could be produced by the parallel connection of $GePt_3$-based DSSCs of larger reaction area. Thus, it is believed that a module containing 25 or above series-connected cells has the potential to increase the open-circuit voltage to 12 V, which can possibly drive an automobile in the future.

Similar to solar energy, hydrogen energy is also known as an important renewable energy source. We also conducted more experiments to evaluate the application of Ge–Pt nanoparticles as the catalyst of the working electrode for the hydrogen evolution reaction (HER). HER is the cathodic half reaction of water splitting ($2H_2O \rightarrow 2H_2 + O_2$), and it is one of the most well-studied electrochemical reactions. The electrocatalytic HER activity of the as-synthesized $GePt_3$ nanoparticles deposited on a glassy carbon electrode was investigated in 0.5 M H_2SO_4 electrolyte ($2H_{(aq)}^+ + 2e^- \rightarrow H_{2(g)}$) using a typical three-electrode system at room temperature. In a solar water splitting system, the HER current density of 10 mA cm^{-2} cathode is assumed as a significant performance index as it is the current density expected for a 12.3% efficient solar water-splitting device.[62] From this perspective, for the linear sweep voltammetry (LSV) measurement, we compared the HER activities of $GePt_3$ and Ge_2Pt with that of commercial 20 wt% Pt/C, and the results are summarized as Fig. 8(a). However, Ge_2Pt nanoparticles resulted in a very poor HER catalytic activity or they were merely non-reactive. Subsequently, a series of HER activity tests based on $GePt_3$ were conducted at different HER reactive areas, and the resultant HER activities of $GePt_3$ nanoparticles were comparable to those of Pt/C at a current density of 10 mA cm^{-2} (Table 3). As shown in Table 3, HER of the $GePt_3$ electrode at a larger area (5 cm^2) required a higher overpotential (0.081 V) to achieve a current density of 10 mA cm^{-2}. We tried to improve the performance of the catalyst by activating it with a stable potential of 0.1 V for 10 minutes to remove the possible surface contaminants, and the HER activity at 5 cm^2 was reevaluated. As expected, the result improved with an overpotential reduction from 0.081 V to 0.053 V. To probe the HER kinetics, Tafel slopes were calculated. As depicted in Fig. 8(b), the Tafel slopes were 51.1 mV per decade for Pt/C and 40.7 mV per

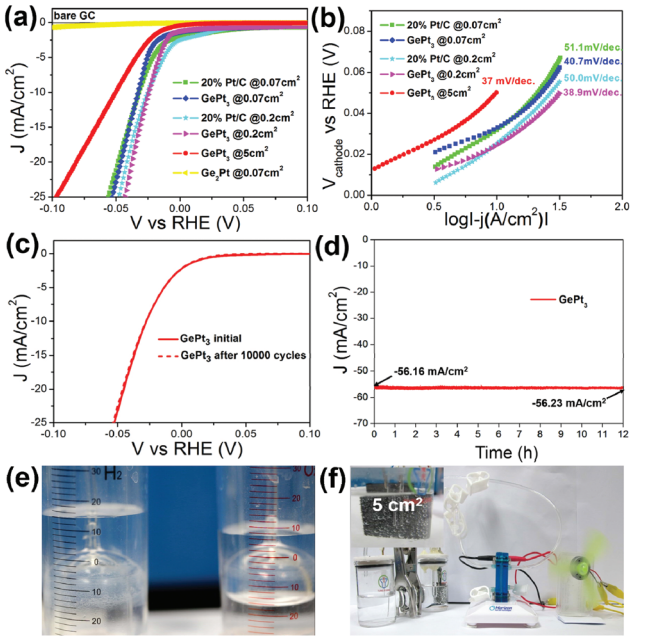

Fig. 8 (a) Representative polarization curves of $GePt_3$ and 20% Pt/C on working electrodes of different areas; (b) corresponding Tafel plots, (c) polarization curves of $GePt_3$ initially and after 10 000 CV scans, (d) amperometric *i*–*t* curve of $GePt_3$ with an applied voltage of −0.1 V *vs.* RHE over 12 hours in 0.5 M H_2SO_4 electrolyte. (e) Result of the water displacement method to collect hydrogen and oxygen gas. (f) Equipment for HER demonstration including a three electrode system cell, a fuel cell and an electric fan.

Table 3 Electrochemical performances of 0.07, 0.2, 5 cm^2 areas with Pt/C and $GePt_3$ working electrode, showing the overpotential result for −10 mA cm^{-2} when applied for hydrogen evolution

	0.07 cm^2	0.2 cm^2	5 cm^2	5 cm^2-actived
20% Pt/C	0.032	0.025	—	—
$GePt_3$	0.033	0.024	0.081	0.053

decade for $GePt_3$ at 0.07 cm^2. The HER area was then enlarged to 0.2 cm^2, and the resultant Tafel slopes were 50.0 mV per decade for Pt/C and 38.9 mV per decade for $GePt_3$. It was remarkable that the activated $GePt_3$ electrocatalyst could still yield a Tafel slope of 37 mV per decade even at a large HER reactive area (5 cm^2), indicating significant electrocatalytic activity towards HER with the Volmer–Heyrovsky mechanism.[63]

Pt-Related compounds can serve as electrocatalysts in alkaline or acidic electrolytes.[64–66] In addition to overpotential, stability is one of the most important factors to estimate an electrocatalyst.[67] Next, we evaluated the electrochemical durability of $GePt_3$ *via* a cycling test by running continuous CVs between 0.2 and −0.3 V (*vs.* RHE) at a scan rate of 120 mV s^{-1} for 10 000 cycles (Fig. 8(c)); the overlapping curves implied that there was no decrease in the performance after 10 000 cycles. Additionally, as clarified in Fig. 8(d), the chronoamperometry measurement showed that the $GePt_3$ electrocatalyst maintained a stable current density at −0.1 V *vs.* RHE in 0.5 M H_2SO_4 solution for 12 hours. The current density for hydrogen evolution reaction was ~56 mA cm^{-2}, and it remained almost constant throughout the testing period. To further illustrate the intrinsic catalytic activity of $GePt_3$, its specific HER activity and the mass activity at −0.1 V *vs.* RHE were compared with those of commercial Pt black and Pt/C catalysts (Fig. S10†). The total Pt content in the $GePt_3$ electrocatalyst was about 76.4 wt%, which was quantitatively measured by the inductively coupled plasma mass spectrometry (ICP-MS) technique. It showed that the corresponding specific activity of $GePt_3$ was 56.2 mA cm^{-2}, which was larger than those of Pt black (52.7 mA cm^{-2}) and Pt/C (46.9 mA cm^{-2}). Similarly, the mass activity of $GePt_3$ was 367.8 mA mg_{Pt}^{-1}, which was also higher than that of Pt black (263.8 mA mg_{Pt}^{-1}). Notably, the carbon-supported Pt (Pt/C) was able to achieve a relatively high mass activity (1172.5 mA mg_{Pt}^{-1}), indicating that it is possible to dramatically reduce the Pt usage and enhance the HER mass activity of the as-synthesized $GePt_3$ catalyst as long as it is applied with an appropriate support material.

Our experimental results indicated that $GePt_3$ can serve as an excellent electrocatalyst in an acidic solution. Next, we applied the water displacement method to confirm the continuous production of hydrogen during the reaction. The resultant volume ratio of collected hydrogen and oxygen was 2 to 1, yielding the volume ratio of hydrogen and oxygen in a water splitting system (Fig. 8(e)). Finally, the hydrogen gas produced from the HER system was applied directly to a fuel cell system to drive an electric fan (Fig. 8(f) and Movie S3†). During the demonstration, a constant voltage (0.3 V) was applied to the HER system and it could provide sufficient hydrogen to continuously function the fuel cell.

4. Conclusions

In summary, we developed facile colloidal synthesis of $GePt_3$ and Ge_2Pt nanoparticles in a general and well-controlled manner. The properties and applications of the as-synthesized nanoparticles could be influenced by their morphology or composition; $GePt_3$ catalysts demonstrated better performance than Ge_2Pt for both DSSC devices and HER reactions, probably due to their higher molar ratio of active Pt catalysts. Also, the pop-corn shape with uneven surfaces enabled the nanoparticles to provide a larger surface area for the electrochemical catalysis reaction. In the DSSC device application, $GePt_3$ nanoparticle-based counter electrodes with reactive areas of 0.16 and 2 cm^2 resulted in average PCEs of 8.04% and 7.26%, which were comparable to that of Pt electrodes. We successfully achieved the demonstrations of $GePt_3$-based series-connected DSSC applications by driving an electric fan and illuminating an LED array. Further work to explore DSSC modules of advanced design for a higher voltage and a higher current output for a wide range of applications is currently underway. Also, the drop coating method and spray coating method were applied to deposit the as-synthesized nanoparticles onto different substrates as working electrodes for the HER water splitting system. The LSV measurements demonstrated an extremely low value of overpotential (<0.06 V) even at a larger reactive area (5 cm^2). Next, the $GePt_3$-based electrode was applied to a series of tests including cycling durability tests and a fuel cell system demonstration, and the test results verified the prominent stability of the catalyst even after continuously reacting for 10 000 cycles or 12 hours. For the demonstration of the fuel cell system, hydrogen was continuously produced and collected and it could successfully drive an electric fan. All in all, this highly reactive and stable Ge–Pt nanoparticle-based catalyst could serve as a high-performance counter electrode for photoelectric conversions and as a promising candidate material to enable the widespread deployment of cost-effective systems for electrochemical hydrogen production.

Conflicts of interest

There are no conflicts to declare.

Acknowledgements

The authors gratefully acknowledge the financial support by the Ministry of Science and Technology through the grants of NSC 102-2221-E-007-023-MY3, MOST 103-2221-E-007-089-MY3, MOST 103-2622-E-007-025, MOST 102-2633-M-007-002, and MOST 106-2628-E-007-005-MY3.

References

1 R. F. Service, *Science*, 2002, **296**, 1222–1224.
2 J. B. Wu and H. Yang, *Acc. Chem. Res.*, 2013, **46**, 1848–1857.
3 A. Pavlisic, P. Jovanovic, V. S. Selih, M. Sala, M. Bele, G. Drazic, I. Arcon, S. Hocevar, A. Kokalj, N. Hodnik and M. Gaberscek, *ACS Catal.*, 2016, **6**, 5530–5534.

4 X. X. Weng, Y. Liu, K. K. Wang, J. J. Feng, J. H. Yuan, A. J. Wang and Q. Q. Xu, *Int. J. Hydrogen Energy*, 2016, **41**, 18193–18202.
5 G. T. Fu, K. Wu, J. Lin, Y. W. Tang, Y. Chen, Y. M. Zhou and T. H. Lu, *J. Phys. Chem. C*, 2013, **117**, 9826–9834.
6 X. Y. Liu, Y. Zhang, M. X. Gong, Y. W. Tang, T. H. Lu, Y. Chen and J. M. Lee, *J. Mater. Chem. A*, 2014, **2**, 13840–13844.
7 S. Wang, D. Zhang, Y. Ma, H. Zhang, J. Gao, Y. Nie and X. Sun, *ACS Appl. Mater. Interfaces*, 2014, **6**, 12429–12435.
8 S. H. Sun, *Adv. Mater.*, 2006, **18**, 393–403.
9 X. D. Wang, L. Altmann, J. Stover, V. Zielasek, M. Baumer, K. Al-Shamery, H. Borchert, J. Parisi and J. Kolny-Olesiak, *Chem. Mater.*, 2013, **25**, 1400–1407.
10 D. Y. Wang, H. L. Chou, Y. C. Lin, F. J. Lai, C. H. Chen, J. F. Lee, B. J. Hwang and C. C. Chen, *J. Am. Chem. Soc.*, 2012, **134**, 10011–10020.
11 E. V. Shevchenko, D. V. Talapin, A. L. Rogach, A. Kornowski, M. Haase and H. Weller, *J. Am. Chem. Soc.*, 2002, **124**, 11480–11485.
12 S. J. Guo and S. H. Sun, *J. Am. Chem. Soc.*, 2012, **134**, 2492–2495.
13 T. Y. Xia, J. L. Liu, S. G. Wang, C. Wang, Y. Sun, L. Gu and R. M. Wang, *ACS Appl. Mater. Interfaces*, 2016, **8**, 10841–10849.
14 T. Ghosh, B. M. Leonard, Q. Zhou and F. J. DiSalvo, *Chem. Mater.*, 2010, **22**, 2190–2202.
15 T. Ishimoto and M. Koyama, *J. Phys. Chem. Lett.*, 2016, **7**, 736–740.
16 Z. M. Cui, H. Chen, M. T. Zhao, D. Marshall, Y. C. Yu, H. Abruna and F. J. DiSalvo, *J. Am. Chem. Soc.*, 2014, **136**, 10206–10209.
17 X. H. Sun, K. Z. Jiang, N. Zhang, S. J. Guo and X. Q. Huang, *ACS Nano*, 2015, **9**, 7634–7640.
18 Z. Y. Qi, C. X. Xiao, C. Liu, T. W. Goh, L. Zhou, R. Maligal-Ganesh, Y. C. Pei, X. L. Li, L. A. Curtiss and W. Y. Huang, *J. Am. Chem. Soc.*, 2017, **139**, 4762–4768.
19 H. Z. Yang, J. Zhang, K. Sun, S. Z. Zou and J. Y. Fang, *Angew. Chem., Int. Ed.*, 2010, **49**, 6848–6851.
20 D. D. Vaughn and R. E. Schaak, *Chem. Soc. Rev.*, 2013, **42**, 2861–2879.
21 D. J. Xue, J. J. Wang, Y. Q. Wang, S. Xin, Y. G. Guo and L. J. Wan, *Adv. Mater.*, 2011, **23**, 3704–3705.
22 J. Y. Fan and P. K. Chu, *Small*, 2010, **6**, 2080–2098.
23 R. Pillarisetty, *Nature*, 2011, **479**, 324–328.
24 G. P. Felcher, J. D. Jorgensen and R. Wappling, *J. Phys. C: Solid State Phys.*, 1983, **16**, 6281–6290.
25 J. Sato, N. Saito, Y. Yamada, K. Maeda, T. Takata, J. N. Kondo, M. Hara, H. Kobayashi, K. Domen and Y. Inoue, *J. Am. Chem. Soc.*, 2005, **127**, 4150–4151.
26 R. E. Simpson, M. Krbal, P. Fons, A. V. Kolobov, J. Tominaga, T. Uruga and H. Tanida, *Nano Lett.*, 2010, **10**, 414–419.
27 J. Liu, M. Beals, A. Pomerene, S. Bernardis, R. Sun, J. Cheng, L. C. Kimerling and J. Michel, *Nat. Photonics*, 2008, **2**, 433–437.
28 M. T. Currie, S. B. Samavedam, T. A. Langdo, C. W. Leitz and E. A. Fitzgerald, *Appl. Phys. Lett.*, 1998, **72**, 1718–1720.
29 H. Okamoto, *J. Phase Equilib.*, 1992, **13**, 413.
30 A. Borgna, T. F. Garetto, C. R. Apesteguia and B. Moraweck, *Appl. Catal., A*, 1999, **182**, 189–197.
31 I. M. J. Vilella, S. R. de Miguel and O. A. Scelza, *J. Mol. Catal. A: Chem.*, 2008, **284**, 161–171.
32 E. M. Crabb and M. K. Ravikumar, *Electrochim. Acta*, 2001, **46**, 1033–1041.
33 T. Komatsu, S. Hyodo and T. Yashima, *J. Phys. Chem. B*, 1997, **101**, 5565–5572.
34 N. Gyorffy, I. Bakos, S. Szabo, L. Toth, U. Wild, R. Schlogl and Z. Paal, *J. Catal.*, 2009, **263**, 372–379.
35 H. J. Yang, S. Y. He, H. L. Chen and H. Y. Tuan, *Chem. Mater.*, 2014, **26**, 1785–1793.
36 S. C. Lu, M. C. Hsiao, M. Yorulmaz, L. Y. Wang, P. Y. Yang, S. Link, W. S. Chang and H. Y. Tuan, *Chem. Mater.*, 2015, **27**, 8185–8188.
37 N. T. K. Thanh, N. Maclean and S. Mahiddine, *Chem. Rev.*, 2014, **114**, 7610–7630.
38 X. Q. Huang, E. B. Zhu, Y. Chen, Y. J. Li, C. Y. Chiu, Y. X. Xu, Z. Y. Lin, X. F. Duan and Y. Huang, *Adv. Mater.*, 2013, **25**, 2974–2979.
39 T. Yang, Y. X. Ma, Q. L. Huang and G. J. Cao, *Nano Energy*, 2016, **19**, 257–268.
40 Q. Wang, Q. Zhao, Y. G. Su, G. Zhang, G. R. Xu, Y. J. Li, B. C. Liu, D. F. Zheng and J. Zhang, *J. Mater. Chem. A*, 2016, **4**, 12296–12307.
41 J. Y. Zheng, G. Song, J. S. Hong, T. K. Van, A. U. Pawar, D. Y. Kim, C. W. Kim, Z. Haider and Y. S. Kang, *Cryst. Growth Des.*, 2014, **14**, 6057–6066.
42 J. F. Xie, H. Zhang, S. Li, R. X. Wang, X. Sun, M. Zhou, J. F. Zhou, X. W. Lou and Y. Xie, *Adv. Mater.*, 2013, **25**, 5807–5808.
43 Z. Luo, R. Miao, T. D. Huan, I. M. Mosa, A. S. Poyraz, W. Zhong, J. E. Cloud, D. A. Kriz, S. Thanneeru, J. K. He, Y. S. Zhang, R. Ramprasad and S. L. Suib, *Adv. Energy Mater.*, 2016, **6**, 1600528.
44 T. P. Bigioni, X. M. Lin, T. T. Nguyen, E. I. Corwin, T. A. Witten and H. M. Jaeger, *Nat. Mater.*, 2006, **5**, 265–270.
45 A. P. LaGrow, B. Ingham, S. Cheong, G. V. M. Williams, C. Dotzler, M. F. Toney, D. A. Jefferson, E. C. Corbos, P. T. Bishop, J. Cookson and R. D. Tilley, *J. Am. Chem. Soc.*, 2012, **134**, 855–858.
46 T. Ishizaki, K. Yatsugi and K. Akedo, *Nanomaterials*, 2016, **6**, 172.
47 M. Yang, T. P. Chen, J. I. Wong, Y. Liu, L. Ding, K. Y. Liu, S. Zhang, W. L. Zhang, D. Gui and C. Y. Ng, *J. Phys. D: Appl. Phys.*, 2009, **42**, 035109.
48 D. Xiang and L. W. Yin, *J. Mater. Chem.*, 2012, **22**, 9584–9593.
49 K. Prabhakaran and T. Ogino, *Surf. Sci.*, 1995, **325**, 263–271.
50 Z. Paal, U. Wild, A. Wootsch, J. Find and R. Schlogl, *Phys. Chem. Chem. Phys.*, 2001, **3**, 2148–2155.

51 R. Chivas, S. Yerci, R. Li, L. Dal Negro and T. F. Morse, *Opt. Mater.*, 2011, **33**, 1829–1832.
52 Y. J. Zhang, Y. Y. Zhao, H. Zhang, L. Y. Zhang, H. P. Ma, P. P. Dong, D. S. Li, J. J. Yu and G. Y. Cao, *RSC Adv.*, 2016, **6**, 70653–70659.
53 D. J. Chen, Z. Y. Zhou, Q. Wang, D. M. Xiang, N. Tian and S. G. Sun, *Chem. Commun.*, 2010, **46**, 4252–4254.
54 Q. G. Zhai, S. J. Xie, W. Q. Fan, Q. H. Zhang, Y. Wang, W. P. Deng and Y. Wang, *Angew. Chem., Int. Ed.*, 2013, **52**, 5776–5779.
55 M. Koshino and T. Ando, *Solid State Commun.*, 2009, **149**, 1123–1127.
56 G. Giovannetti, P. A. Khomyakov, G. Brocks, V. M. Karpan, J. van den Brink and P. J. Kelly, *Phys. Rev. Lett.*, 2008, **101**, 026803.
57 A. I. Popov and D. H. Geske, *J. Am. Chem. Soc.*, 1958, **80**, 1340–1352.
58 M. K. Wang, A. M. Anghel, B. Marsan, N. L. C. Ha, N. Pootrakulchote, S. M. Zakeeruddin and M. Gratzel, *J. Am. Chem. Soc.*, 2009, **131**, 15976–15977.
59 C. P. Hsu, K. M. Lee, J. T. W. Huang, C. Y. Lin, C. H. Lee, L. P. Wang, S. Y. Tsai and K. C. Ho, *Electrochim. Acta*, 2008, **53**, 7514–7522.
60 A. Subramanian and H. W. Wang, *Appl. Surf. Sci.*, 2012, **258**, 6479–6484.
61 T. Schmidt, F. Gartner, H. Assadi and H. Kreye, *Acta Mater.*, 2006, **54**, 729–742.
62 M. G. Walter, E. L. Warren, J. R. McKone, S. W. Boettcher, Q. X. Mi, E. A. Santori and N. S. Lewis, *Chem. Rev.*, 2010, **110**, 6446–6473.
63 G. H. Carey, A. L. Abdelhady, Z. J. Ning, S. M. Thon, O. M. Bakr and E. H. Sargent, *Chem. Rev.*, 2015, **115**, 12732–12763.
64 C. Chen, Y. J. Kang, Z. Y. Huo, Z. W. Zhu, W. Y. Huang, H. L. L. Xin, J. D. Snyder, D. G. Li, J. A. Herron, M. Mavrikakis, M. F. Chi, K. L. More, Y. D. Li, N. M. Markovic, G. A. Somorjai, P. D. Yang and V. R. Stamenkovic, *Science*, 2014, **343**, 1339–1343.
65 Q. Li, L. H. Wu, G. Wu, D. Su, H. F. Lv, S. Zhang, W. L. Zhu, A. Casimir, H. Y. Zhu, A. Mendoza-Garcia and S. H. Sun, *Nano Lett.*, 2015, **15**, 2468–2473.
66 L. Dai, Y. Zhao, Q. Qin, X. J. Zhao, C. F. Xu and N. F. Zheng, *ChemNanoMat*, 2016, **2**, 776–780.
67 X. R. Liu, M. Zhang, T. T. Yang, L. N. Wang, H. Zhu, S. L. Wang and M. L. Du, *Mater. Des.*, 2016, **109**, 162–170.

